Ionized gas kinematics in bipolar HII regions

Hannah S. Dalgleish,[1]★ Steven N. Longmore,[1] Thomas Peters,[2]
Jonathan D. Henshaw,[1,3] Joshua L. Veitch-Michaelis[4] and James S. Urquhart[5]

[1]*Astrophysics Research Institute, Liverpool John Moores University, Liverpool L3 5RF, UK*
[2]*Max-Planck-Institut für Astrophysik, Karl-Schwarzschild-Str. 1, D-85748 Garching, Germany*
[3]*Max-Planck-Institut für Astronomie, Königstuhl 17, D-69117 Heidelberg, Germany*
[4]*I3D Robotics Ltd, Tonbridge TN9 1SP, UK*
[5]*Centre for Astrophysics and Planetary Science, University of Kent, Canterbury CT2 7NH, UK*

ABSTRACT

Stellar feedback plays a fundamental role in shaping the evolution of galaxies. Here, we explore the use of the ionized gas kinematics in young, bipolar HII regions as a probe of early feedback in these star-forming environments. We have undertaken a multiwavelength study of a young, bipolar HII region in the Galactic disc, G316.81–0.06, which lies at the centre of a massive ($\sim 10^3$ M$_\odot$) infrared dark cloud filament. It is still accreting molecular gas as well as driving a ~ 0.2 pc ionized gas outflow perpendicular to the filament. Intriguingly, we observe a large velocity gradient (47.81 ± 3.21 km s^{-1} pc^{-1}) across the ionized gas in a direction perpendicular to the outflow. This kinematic signature of the ionized gas shows a reasonable correspondence with the simulations of young H II regions. Based on a qualitative comparison between our observations and these simulations, we put forward a possible explanation for the velocity gradients observed in G316.81−0.06. If the velocity gradient perpendicular to the outflow is caused by the rotation of the ionized gas, then we infer that this rotation is a direct result of the initial net angular momentum in the natal molecular cloud. If this explanation is correct, this kinematic signature should be common in other young (bipolar) HII regions. We suggest that further quantitative analysis of the ionized gas kinematics of young H II regions, combined with additional simulations, should improve our understanding of feedback at these early stages.

Key words: stars: kinematics and dynamics – stars: massive – stars: protostars – H II regions.

1 INTRODUCTION

Feedback from high-mass stars (i.e. OB stars with $M_\star \geq 8$ M$_\odot$) is fundamental to the shaping of the visible Universe. From the moment star formation begins, stellar feedback commences, injecting energy and momentum into the natal environment. This feedback can both hinder and facilitate star formation; negative feedback restrains or can even terminate star formation, whereas positive feedback acts to increase the star formation rate and/or efficiency. Many different physical mechanisms contribute to feedback by varying degrees, each depending on a variety of factors (e.g. initial conditions), resulting in an intricate and interdependent series of processes. In a recent review on this topic, Krumholz et al. (2014) group feedback processes into three main categories: momentum feedback (e.g. protostellar outflows and radiation pressure), explosive feed-back (e.g. stellar winds, photoionizing radiation, and supernovae), and thermal feedback (e.g. non-ionizing radiation).

Stellar feedback encompasses many astrophysical processes, moderating star formation from stellar scales ($\ll 1$ pc) to cosmological kpc scales (e.g. driving Galactic outflows; Murray, Ménard & Thompson 2011; Girichidis et al. 2016). Despite our growing knowledge of these processes, the overarching interplay between them remains uncertain. Observationally, limited spatial resolution makes it difficult to disentangle the effects of feedback mechanisms, which operate simultaneously. Other additional factors, such as the role of magnetic fields (for which the strength and orientation are difficult to measure) and feedback from surrounding low-mass stars, complicate the process further. Moreover, limited observations of the earliest stages of high-mass star formation means that the large samples needed for a robust statistical analysis are lacking. With observatories such as ALMA and the EVLA, which have sufficient angular resolution to resolve and detect individually forming high-mass stars, our understanding is continually improving.

★ E-mail: h.s.dalgleish@2016.ljmu.ac.uk

Meanwhile, in the past few decades, there have been considerable efforts attempting to simulate the vast range of stellar feedback effects. It has been clearly demonstrated that without feedback, simulations fail to replicate the galaxies that we observe in the Universe today (e.g. Katz, Weinberg & Hernquist 1996; Somerville & Primack 1999; Cole et al. 2000; Springel & Hernquist 2003; Kereš et al. 2009; Girichidis et al. 2011; Kennicutt & Evans 2012; Scannapieco et al. 2012; Hopkins et al. 2014; Peters et al. 2017) and often produce galaxies that are much more massive than observed. Consequently, simulations have looked to feedback for answers, with promising results. Yet it remains a great challenge to create a model that includes all feedback processes over a vast range of scales. Often only one or two types of feedback are included (e.g. Krumholz et al. 2010; Myers et al. 2011; Dale, Agertz et al. 2013; Ercolano & Bonnell 2013; Kim, Ostriker & Kim 2013; Peters et al. 2014; Tasker, Muratov et al. 2015; Wadsley & Pudritz 2015; Agertz & Kravtsov 2016; Butler et al. 2017; Núñez et al. 2017). In order to improve simulations and implement more feedback effects, better understanding of the relevant physical processes is needed. This will help to provide the observational constraints needed for parametrizing the simulations.

1.1 H II regions

The study of H II regions can allow us to explore how high-mass stars impact their environment via the aforementioned feedback mechanisms. H II regions are bright in the radio regime, particularly with radio recombination lines (RRLs) and thermal bremsstrahlung, both clear diagnostics of high-mass star formation. See Haworth et al. (2017) for a review on synthetic observation studies, particularly regarding feedback and the global structure of H II regions.

Predominantly, the study of H II regions has focused on surveys examining morphologies, sizes, and densities (e.g. Helfand et al. 2006; Hoare et al. 2012; Urquhart et al. 2013a,b; Giannetti et al. 2017; Kim et al. 2017). In terms of morphology, ultra compact (UC; ≤0.1 pc) H II regions can be categorized as either spherical, cometary, core halo, shell or irregular (Wood & Churchwell 1989). de Pree et al. (2005) modified the classification scheme to also include bipolar morphologies. The work of Wood & Churchwell (1989) found that too many UCH II regions are observed considering their short apparent lifetime, known as the 'lifetime debate'. Peters et al. (2010b) propose a solution based on their synthetic radio continuum observations of young high-mass star formation regions. They found that H II regions 'flicker' as they grow, a result of a fluctuating accretion flow around the high-mass star (fragmentation-induced starvation; Peters et al. 2010a, hereafter P10). This is a possible resolution to the lifetime problem since the young H II regions shrink and grow rapidly as they evolve. Short (several year) variations in the flux density of the high-mass star-forming region Sgr B2 have been observed (de Pree et al. 2014, 2015), which the authors attribute to this 'flickering'.

There have also been detailed studies on the kinematics of H II regions on (proto)stellar scales (≲10 000 au). This includes the accretion of ionized material on to forming high-mass stars (e.g. Keto, Ho & Haschick 1988; Keto 2002, 2003, 2007; Sollins et al. 2005; Keto & Wood 2006; Galván-Madrid et al. 2008; Keto & Klaassen 2008; Klaassen et al. 2018); the gravitational collapse and rotation of turbulent molecular clouds (e.g. Klessen, Heitsch & Mac Low 2000; Klaassen et al. 2009); ionized outflows (e.g. de Pree et al. 1994; Klaassen et al. 2013; Tanaka, Tan & Zhang 2016); and the rotation of the ionized gas on stellar scales (e.g. Rodriguez & Bastian 1994; Sewiło et al. 2008).

However, to date, fewer studies have been devoted to measuring the ionized gas kinematics of H II regions on cloud scales (∼0.1 pc), pertinent to understanding the effect of feedback of high-mass stars on their natal clouds. Most studies have focused on understanding the kinematics of cometary H II regions in order to deduce which model (e.g. bow shock or champagne) applies. This is often done via the analysis of velocity ranges or gradients of the ionized gas (e.g. Lumsden & Hoare 1996, 1999; Veena et al. 2017). Intriguingly, G34.3+0.2, G45.07+0.13, and an Sgr B2 I and H all show ranges in velocity (from 10 to 35 km s^{-1}), perpendicular to the axis of symmetry of the cometary H II region (Garay, Rodriguez & van Gorkom 1986; Gaume & Claussen 1990; Gaume, Fey & Claussen 1994; Immer et al. 2014).

Kinematic studies of H II regions across all morphological types could present new interpretations on our understanding of feedback. For example, bipolar H II regions could provide an insight to early feedback, since they typically exist at earlier evolutionary stages when ionization has only just begun (e.g. Battersby et al. 2010). Newly ionized material flows outwards with velocities up to 30 km s^{-1} (Deharveng et al. 2015) and neutral material (usually in the form of a molecular disc) lies perpendicular to the outflows, often showing signs of accretion towards a central (proto)star. When viewed approximately edge on, the H II region appears bipolar. Velocity gradients within the ionized gas will typically correspond to infall, outflow, rotation, or a combination, which will be influenced by the viewing angle. This can have different implications for feedback, depending on which motion truly occurs.

In this paper, we present observations of a young, bipolar H II region, G316.81–0.06. Our results show a velocity gradient in the ionized gas at 0.1-pc scales, perpendicular to the bipolar axis. In conjunction with the P10 simulations, we aim to understand the origin of the velocity structure in the ionized gas and its relation to feedback. Section 2 describes the observations and simulations in more detail, followed by the data analysis in Section 3. The results and discussion are in Sections 4 and 5, concluding with a summary in Section 6.

2 DATA

2.1 Observations

Fig. 1 illustrates multiwavelength images of G316.81–0.06, located 2.6 kpc away in the Galactic Disc (Green & McClure-Griffiths 2011; note that this is a newer distance estimate as opposed to the measurement of 2.7 kpc used in the previous literature). Various authors have discussed the kinematic distance ambiguity in relation to this source (Shaver et al. 1981; Busfield et al. 2006; Hou & Han 2014) and conclude it is at the near kinematic distance.

The top infrared (IR) image of Fig. 1 is a *Spitzer* GLIMPSE/MIPSGAL image in the 3.6, 8.0, and 24.0 μm IRAC bands (Benjamin et al. 2003; Carey et al. 2009; Churchwell et al. 2009; Christensen et al. 2012; Gutermuth & Heyer 2015). On the bottom-right, a close-up of G316.81–0.06 of the same GLIMPSE/MIPSGAL image is shown. The region is enlarged further in the bottom-left; a mid-infrared (MIR; 3.6, 4.5, and 8.0μm) GLIMPSE image.

On large scales, strong absorption is featured roughly SE–NW in both IR images, i.e. infrared dark clouds (IRDCs; e.g. Egan et al. 1998). Emission features (MIR bright bubbles) are seen to the north and south, with one distinct and bright MIR central source found at the apex of these two bubbles. Using the *Australian Telescope Compact Array*, two radio-continuum sources classified as UCH II
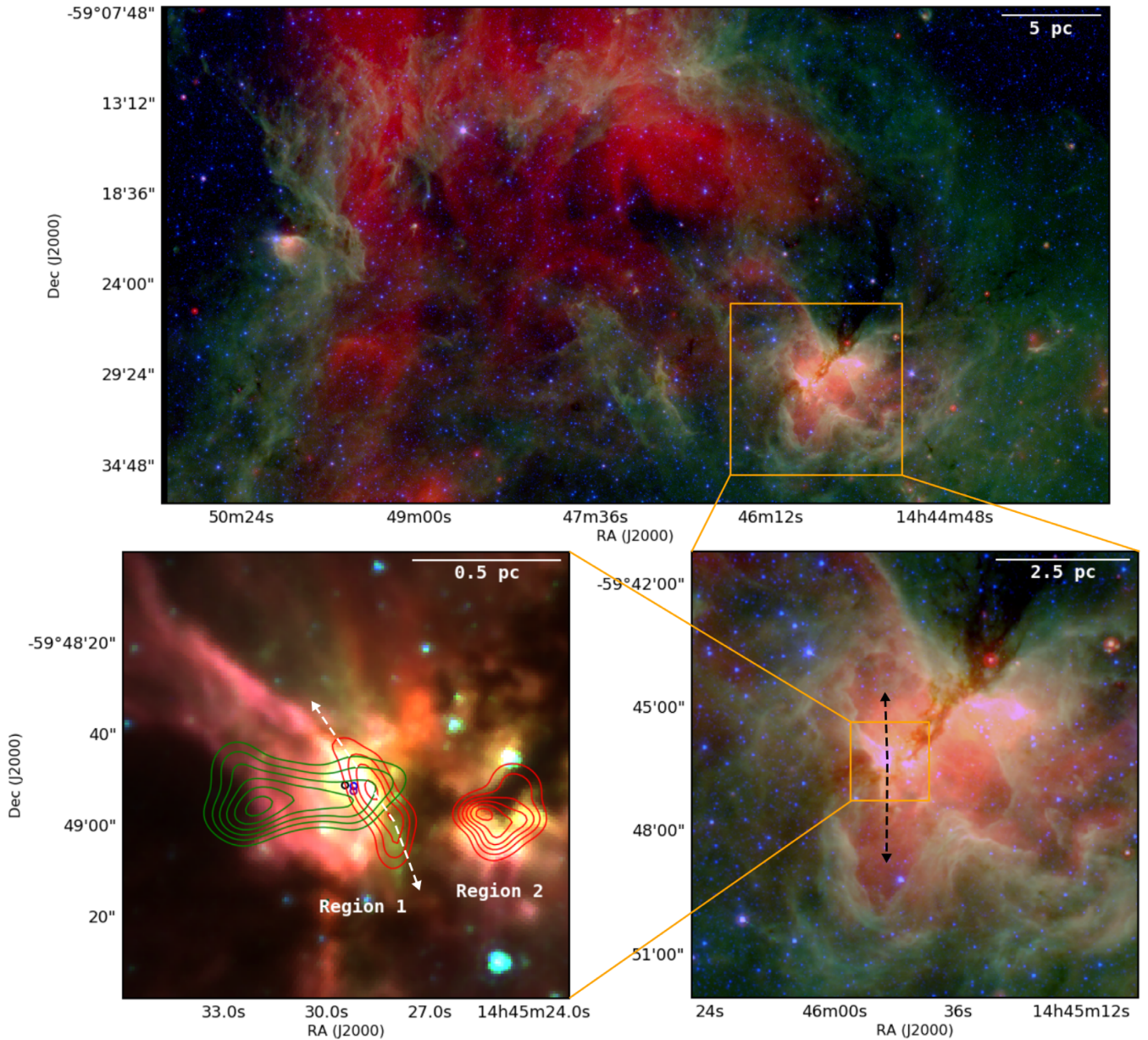
Figure 1. Multiwavelength images of G316.81–0.06. Top and bottom-right: *Spitzer* GLIMPSE/MIPSGAL image in 3.6, 8.0, and 24.0 μm IRAC bands (Benjamin et al. 2003; Carey et al. 2009; Churchwell et al. 2009; Christensen et al. 2012; Gutermuth & Heyer 2015). The dashed black arrows indicate an outflow in the direction of the two north–south MIR bubbles. Bottom-left: GLIMPSE image in 3.6, 4.5, and 8.0 μm IRAC bands (Benjamin et al. 2003; Churchwell et al. 2009). Red and green contours show the 35-GHz continuum (Longmore et al. 2009) and integrated NH$_3$ (1,1; Walsh et al. 1997), respectively. Two separate H II regions are labelled Region 1 and 2 accordingly. Masers from Breen et al. (2010b) are depicted as circles: blue (hydroxyl); black (water); purple (methanol). The dashed white arrows indicate the direction of an ionized outflow, aligned with the 35-GHz continuum of Region 1 and the 'green fuzzy'.

regions in Walsh et al. (1997, 1998) are overlaid with red contours (bottom-left image) showing the 35-GHz continuum (Longmore et al. 2009). The left-hand source (Region 1), shows two distinct lobes elongated roughly NE–SW. The continuum data were taken in addition to the H70α RRL with a compact antenna configuration (12.5 arcsec angular resolution) and thus, spatial filtering is not a major issue (see Longmore et al. 2009 for further details).

Region 1 has many more significant features. Numerous masers (hydroxyl, class II methanol, and water) have been detected, see Appendix A1 for a complete list. For clarity, only the masers listed by Breen et al. (2010b) are marked (bottom-left of Fig. 1): blue, purple, and black circles are hydroxyl, class II methanol, and

water masers, respectively. Ammonia emission (green contours; Walsh et al. 1997) coincides with the three masers, and NH$_3$ (1,1) shows a clear inverse P-Cygni profile towards the cm-continuum source that extends eastwards from Region 1 and peaks towards the IRDC (Longmore et al. 2007). Other features include 4.5 μm excess emission, i.e. a 'green fuzzy' (otherwise known as an extended green object, Cyganowski et al. 2008) in the MIR (bottom-left of Fig. 1; Beuther et al. 2007; Beuther, Walsh & Longmore 2009).

Overall, G316.81–0.06 is a very complex region, affected by contributions from multiple feedback mechanisms. We interpret the aforementioned features as follows: (a) Two MIR bright sources are two separate H II regions (Regions 1 and 2) – formed from the

IRDC filament – which drive the MIR bubbles. It appears as though these cavities have been driven by an older outflow (indicated by the dashed black arrows; bottom-right of Fig. 1) in a north–south direction, perpendicular to the elongated ammonia emission. (b) Masers indicate youth (class II 6.7-GHz maser emission suggests a possible age of 10–45 kyr; Breen et al. 2010a). (c) The inverse P-Cygni profile implies infall towards Region 1. (d) We infer a more recent outflow from the presence of the 'green fuzzy' (Chambers et al. 2009). In combination with the elongated 35-GHz continuum, the outflow appears to be bipolar, possibly in the form of an ionized jet (indicated by the dashed white arrows; bottom-left of Fig. 1).

In contrast, Region 2 lacks masers and ammonia emission. This implies that Region 2 is older than Region 1, as concluded by Longmore et al. (2007).

2.2 Numerical simulations

To help interpret our data, we looked for numerical simulations of young HII regions that match Region 1 as closely as possible. As described next, we identified the simulations of P10 as having global properties similar to G316.81–0.06, so we focus on comparing our data to these simulations. The P10 simulations have not been fine-tuned to the observations.

Given our limited knowledge of the G316.81–0.06 region's history, and with only a single observational snapshot of the region's evolution, it is impossible to know how closely the initial conditions of the simulations are matched to the progenitor gas cloud of G316.81–0.06. For that reason our approach is to try and identify general trends in the evolution of the simulations in the hope that the underlying physical mechanisms driving this evolution will be applicable to the largest number of real HII regions. We avoid focusing on detailed comparison of observations to individual (hyper/UC) HII regions around forming stars in the simulation, for which the evolution is much more stochastic.

Whilst the comparisons between our observations and the simulations of P10 provide a good foundation for further analysis, it would be beneficial to make additional comparisons with a suite of simulations. Such simulations could be fine-tuned to match the observations and model the formation and evolution of HII regions with the same global properties and in the same environment, with a range of different initial conditions. However, this is outside the scope of the paper.

RADMC-The hydrodynamical simulations of P10 describe the gravitational collapse of a rotating molecular gas cloud to form a cluster of massive stars. The 3D model takes into account heating by ionizing and non-ionizing radiation using an adapted FLASH code (Fryxell et al. 2000). The synthetic RRL maps of the simulation data are produced using 3D (Dullemond et al. 2012) as described in Peters, Longmore & Dullemond (2012). Both local thermodynamic equilibrium (LTE) and non-LTE simulations of H70α emission are run for a total of 0.75 Myr. We use RRL data corresponding to 730.4, 739.2, 746.3, 715.3, and 724.7 kyr for which an ionized bubble has already emerged.

Summarizing Peters et al. (2010a,c), the simulated box has a diameter of 3.89 pc with a resolution of 98 au. The initial cloud mass is 1000 $M_\odot$, with an initial temperature of 30 K, and core density 3.85×10^3 cm^{-3}. Beyond the flat inner region of the cloud (0.5-pc radius), the density drops as $r^{-3/2}$. The initial velocities are pure solid-body rotation without turbulence, with angular velocity 1.5×10^{-14} s^{-1}, and a ratio of the rotational energy to gravitational energy, $\beta = 0.05$. Sink particles (of radius 590 au) form when the local density exceeds the critical density, $\rho_{\rm crit} = 2.12 \times 10^8$ cm^{-3}

and the surrounding region around the sink particle, $r_{\rm sink} = 590$ au, is gravitationally bound and collapsing. The sink particles accrete overdense gas that is gravitationally bound, above the threshold density, and within an accretion radius. The accretion rate varies with time and is different for each sink particle. Within the first 10^5 yr since the formation of the first sink particle, the original star has accreted 8 $M_\odot$ and many new sink particles have formed. In the next 3×10^5 yr, the initial three sink particles have masses of 10–20 $M_\odot$, and no star reaches a mass greater than 25 $M_\odot$ overall.

Figs 2 and 3 show density slices of the simulation, for the last 100 kyr. The vectors indicate velocity and the white points represent sink particles. Fig. 2 shows four snapshots equivalent to the initial evolutionary stages before the HII region forms, occurring at 614.0, 624.3, 652.7, and 668.2 kyr. Initially, the cloud looks square as a consequence of not including turbulence in the initial conditions and the use of a grid-based code. The central rarefaction and surrounding dense, ring-like structure may be a result of the cloud undergoing a rotational bounce (i.e. when the core – formed after the collapse of a rotating cloud – continually accretes from the envelope and then expands due to rotation and the increased gas pressure gradient, resulting in a ring at the cloud's centre; Cha & Whitworth 2003). Fig. 3 shows the snapshots at the final stages of the run after the HII region has formed, at 730.4, 739.3, and 746.3 kyr. The thin white border encloses a region that has surpassed a 90 per cent ionization fraction.

2.3 Observations and simulations compared

It is difficult to make an exact comparison between the observations and simulations, since we cannot observe the gas cloud of G316.81–0.06 at its initial stages. Juvela (1996) calculated the density and cloud mass of G316.81–0.06 in their multitransition CS study, finding a mass of 1060 $M_\odot$ and number density 10^4 cm^{-3}, which is in excellent agreement with the simulations.[1]

We can also estimate the mass and size of the region from the IRDC. Longmore et al. (2017) calculated the mass of the IRDC in G316.752+0.004, a region that encompasses G316.81–0.06. They found a mass of 1.5×10^4 $M_\odot$, however, their distance to the IRDC is highly uncertain. Of the two distances they derive, they adopt the farther distance of 9.8 kpc as opposed to the nearer distance of 2.6 kpc (which is also the distance used here). Using the nearer distance estimate, the mass of the IRDC is ∼1150 $M_\odot$ that is also in agreement with the initial molecular mass of the simulated cloud of P10 (1000 $M_\odot$). Assuming a distance of 2.6 kpc, the masses of the observed and simulated clouds are similar.

The sizes of the observed and simulated regions are also similar. The area encompassing both HII regions within G316.81–0.06 is ∼0.9 pc in diameter, although we realize that the IRDC from which the HII regions formed is certainly larger than this. The initial central condensed structure at 500 kyr of the simulations is 1.3 pc in diameter. From this, we infer that the density of the observations and simulations will also be on the same order of magnitude, in agreement with the aforementioned result of Juvela (1996). Given the similarity between the mass and size of the HII regions, we conclude that it is reasonable to compare the observations to the simulations (bearing in mind the caveats in Section 2.2).

---

[1] The author also identifies a velocity gradient across the CS core. Unfortunately, the value is not specified.
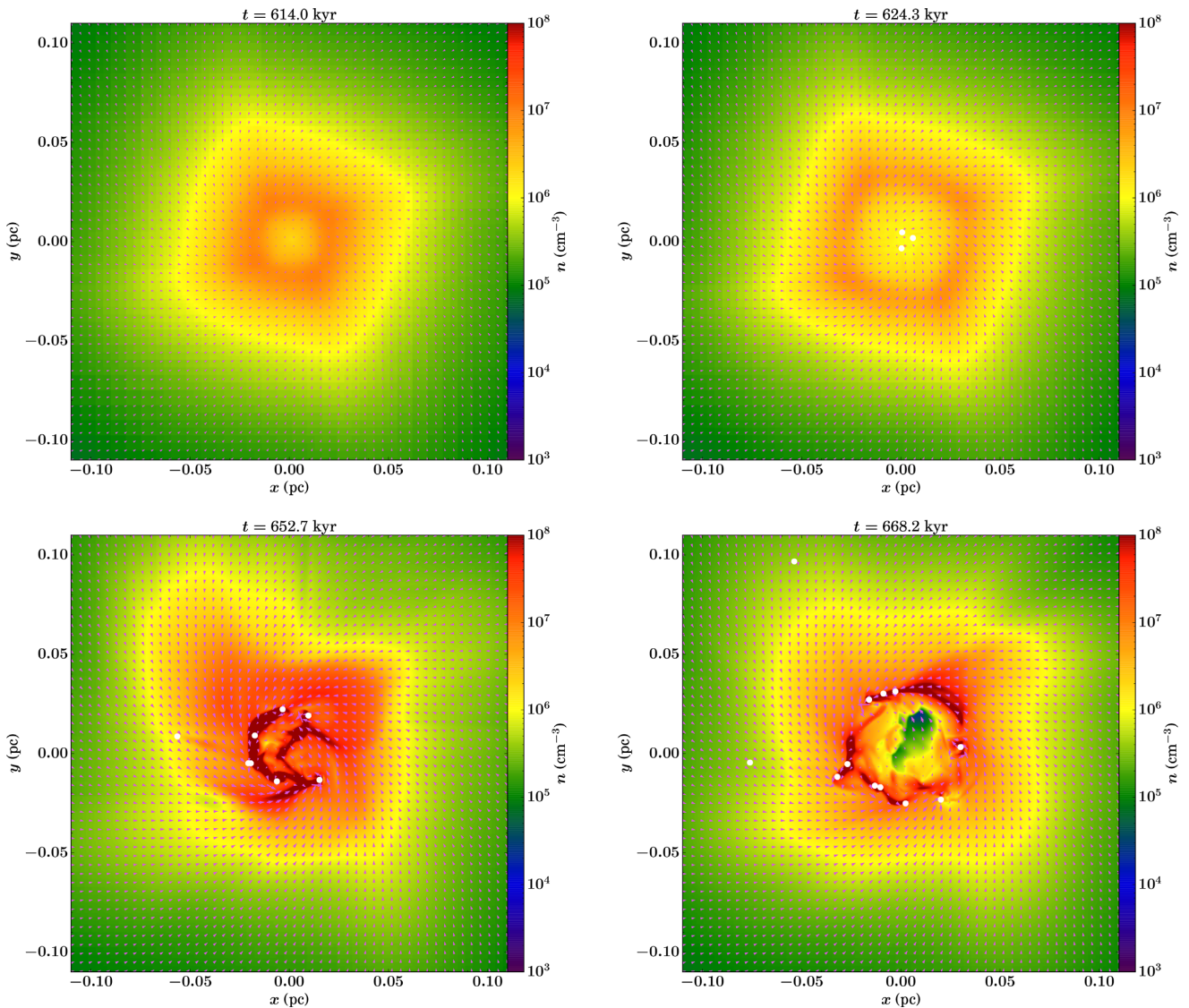
Figure 2. Snapshot density slices through the simulations of P10 depicting the stages prior to the formation of an H II region in the *xy*-plane. The time-steps shown reflect four initial evolutionary stages of the simulation occurring at 614.0, 624.3, 652.7, and 668.2 kyr. The arrows are velocity vectors and the white points are sink particles.

3 DATA ANALYSIS

The data analysis was performed using the Common Astronomy Software Applications (CASA; McMullin et al. 2007) package and the Semi-automated multicomponent Universal Spectral-line fitting Engine (SCOUSE; Henshaw et al. 2016). CASA was used to calculate second moment maps (velocity dispersion, σ), and Gaussians were fit to the spectra using SCOUSE in order to determine centroid velocity (v_0). The input parameters for SCOUSE fitting are found in Table 1, according to Henshaw et al. (2016).

3.1 Observations

We used the H70α RRL spectra taken and reduced by Longmore et al. (2009) for the data analysis. With CASA, the second moment map was created between velocities -9.3 and $-70.7\,\mathrm{km\,s^{-1}}$ including only pixels above $26\,\mathrm{mJy\,beam^{-1}}$ in order to optimally exclude the weaker, second velocity component (see next).

We found that towards the south-west of Region 1, the spectra contain an additional component that is broader (by 14.8 per cent)

and less intense (by 73.5 per cent) than the primary component. Inspection of the data cubes shows that this emission is offset both in velocity and spatially, and we conclude that is unassociated with the ionized gas of Region 1.

Fig. 4 shows Gaussian fits to both components, identified with SCOUSE. Where possible, the contribution of the secondary component was excluded from further analysis, as we are interested in Region 1. At locations where the secondary component is much weaker, it became difficult to distinguish between the two components. This means that we cannot create full width at half-maximum maps reliably, and that the results from the area covering the lowest third of Region 1 must be treated with caution.

3.2 Simulations

In order to compare the simulations and observations more robustly, the units of the H70α synthetic data have been transformed to be consistent with the observations. Intensity was converted from $\mathrm{erg\,s^{-1}\,cm^{-2}\,Hz^{-1}\,ster^{-1}}$ to $\mathrm{Jy\,beam^{-1}}$; physical size converted to
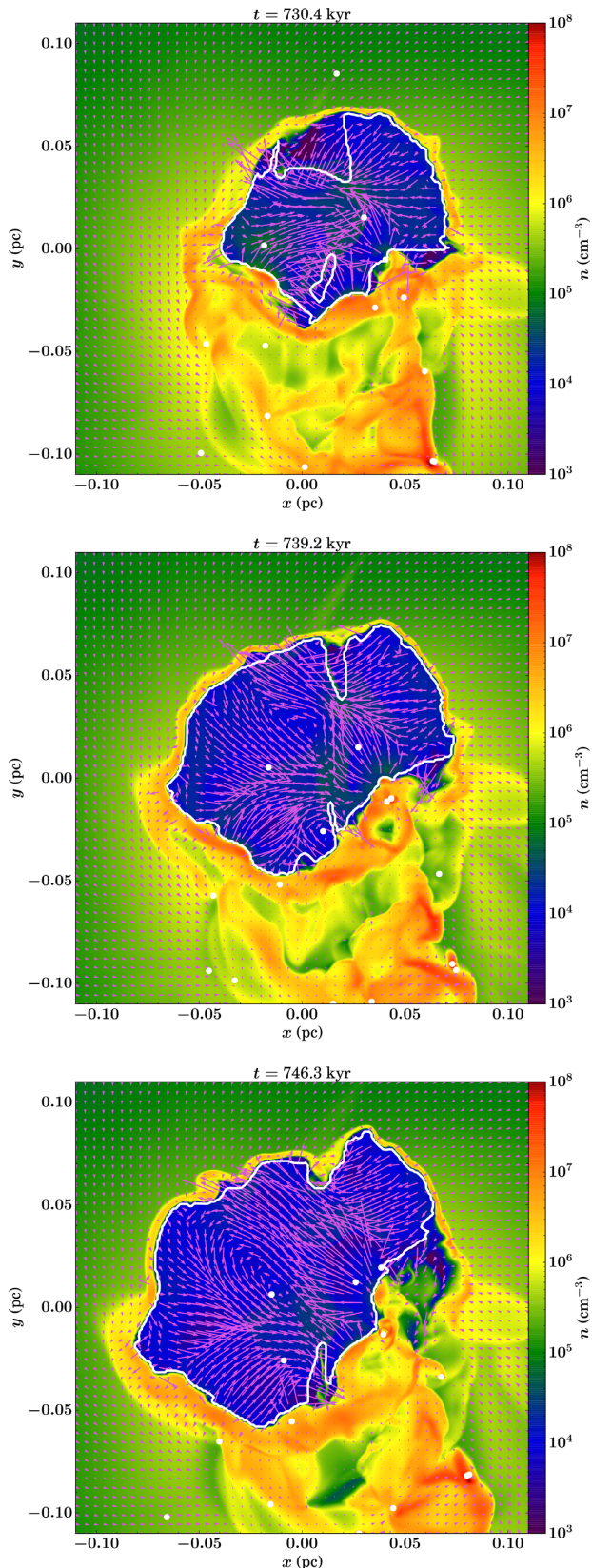
Figure 3. Snapshot density slices through the simulations of P10 after the formation of an H II region in the *xy*-plane. The time-steps reflect later evolutionary stages that occur at 730.4, 739.2, and 746.3 kyr. The arrows depict velocity vectors and the white points are sink particles. The thin white border marks the boundary of 90 per cent ionization fraction.

Table 1. SCOUSE input. Parameter names according to Henshaw et al. (2016).

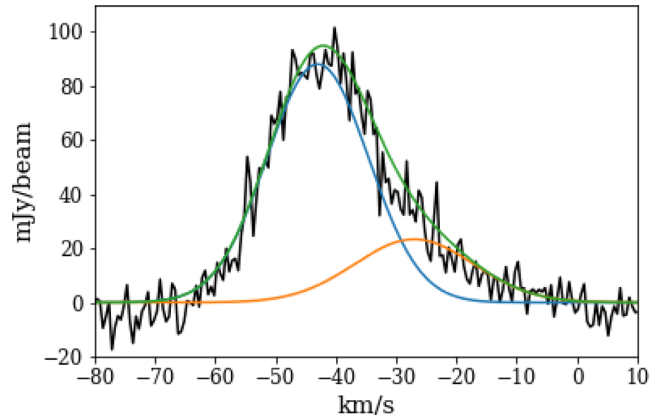| Parameter	Observations	Simulations
R_{SAA}	0″.001	0″.0003
RMS (K)	0.02	0.06
σ_{rms} (K)	3.0	3.0
T_1	5.0	5.0
T_2	2.5	2.5
T_3	2.5	1.7
T_4	1.0	1.00
T_5	0.5	0.5
v_{res} (km s^{-1})	0.5	1.56

Figure 4. H70α spectra of the observational data (Region 1). With SCOUSE, a two-component fit was applied to prevent contamination in further analysis. The primary component (blue) and secondary component (orange) are each fitted by a Gaussian. The combined fit is shown in green.

an angular size using the distance to G316.81–0.06 (2.6 kpc); and frequency converted to velocity. Using CASA, the continuum was subtracted using `imcontsub` with the line-free channels: ≤ 6 and ≥ 54 (LTE); ≤ 10 and ≥ 54 (non-LTE).

A major difference between the LTE and non-LTE simulations were narrow absorption lines (LTE) and very bright, compact, and narrow emission lines (non-LTE) that perhaps emulate real maser emission. In non-LTE conditions, RRLs may undergo maser amplification when the line optical depth is negative and its absolute value is greater than the optical depth of the free–free emission (Gordon & Sorochenko 2002 and references therein). The narrow emission dominates over the broad RRL emission and appears almost as a delta function that prevents SCOUSE from being able to fit the non-LTE simulations. Therefore, a mask was applied to remove the majority of the narrow emission; every value greater than 10 mJy beam^{-1} was replaced with the average of the points on either side.

The narrow absorption lines (LTE) also made SCOUSE fitting difficult. Significant portions of the broad RRL emission were often missing, making it challenging to fit the overall structure. Therefore, the absorption lines were removed via a random sample consensus (RANSAC; Fischler & Bolles 1981) method.[2] RANSAC iteratively estimates the parameters of a mathematical model from a set of data and excludes the effects of outliers. In our case, we selected five points at random (blue circles) along each spectrum (red) to make a Gaussian fit (Fig. 5). Using RANSAC, the best fit is the fit with

[2]For consistency, RANSAC was also applied to the non-LTE data after the narrow emission lines were removed.
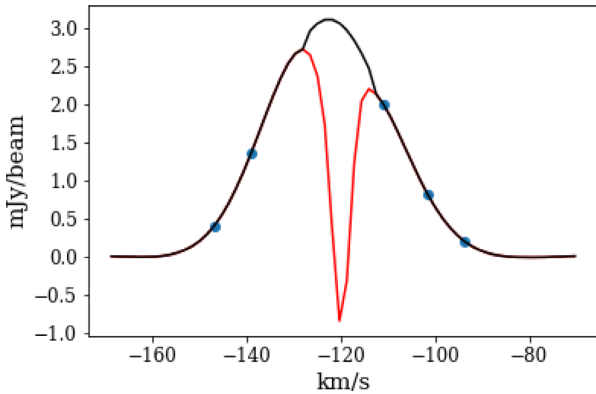
Figure 5. RANSAC example applied to the LTE synthetic data. The narrow absorption lines prevented successful fitting with SCOUSE so they were replaced. The original spectrum (red), the new spectrum (black), and the blue circles represent the five points used to make a Gaussian fit. In this example, this fit was chosen to be the best out of 300 iterations.

the most inliers (points with a residual error of less than 5 per cent) out of 300 iterations. Values of the original spectrum that lay outside the threshold (5 per cent) are replaced by the values from the new fit so as not to entirely eradicate the original data. With this method, we were able to successfully remove the narrow absorption lines without distorting the data, so that we could then proceed with the SCOUSE fitting. This was only successful for the last three time-steps (730.4, 739.2, and 746.3 kyr). At earlier times (715.3 and 724.7 kyr), for which synthetic H70α data are also available, the LTE absorption lines are too wide to be accurately removed via the RANSAC method, and thus cannot be successfully fit by SCOUSE.

Finally, Gaussian smoothing was applied to both the LTE and non-LTE synthetic data with a beam size of 2.5 arcsec, using the `imsmooth` tool in CASA. This is the largest beam size possible while still being able to resolve the overall kinematic structure.

4 RESULTS

Table 2 contains the ranges in velocity (v_0(max)–v_0(min)), velocity gradients, and maximum velocity dispersions for both the observational and synthetic H70α RRL data. Where the observations are concerned, Region 1 is the focus of the study, for it is the youngest H II region (Fig. 6). We note that the velocity gradient measured is what we observe along our line of sight and does not take into account any inclination that may be present. For the simulations (both LTE and non-LTE), we show the results of the final three ages: 730.4, 739.2, and 746.3 kyr in Figs 7 and 8.

4.1 Observed ionized gas kinematics

Fig. 6 contains the H70α centroid velocity and second moment maps for the two H II regions in G316.81–0.06. Several velocity gradients across each region are visible in the centroid velocity map, and we focus on the younger H II region; Region 1 (left). Region 1 shows a velocity gradient roughly east–west (across ~0.33 pc) in addition to a less-steep gradient north–south (across ~0.42 pc) aligned with the elongation of the 35-GHz continuum and 'green fuzzy'. The second moment map shows that in both H II regions σ increases towards the centre and is highest towards the southern end of each region.

4.2 Simulated ionized gas kinematics

Figs 7 and 8 show the centroid velocity and second moment maps of the LTE and non-LTE synthetic H70α data, at the final three ages 730.4, 739.2, and 746.3 kyr. The density slices (Figs 2 and 3) look down on the stars in the *xy*-plane, i.e. along the outflow axis. For the synthetic H70α data, we chose a projection perpendicular to the outflow plane (oriented along the *xz*-plane), to compare with the observations. Although the inclination of the observed Region 1 outflow is not known; Fig. 1 shows it is clearly closer to perpendicular than along the line of sight. Any inclination will introduce a change in the observed velocity motions of order sin(θ), where θ is the angle of inclination.

The velocity structure of the simulated ionized gas on 0.05-pc scales changes insignificantly between the different time-steps for either the non-LTE or LTE synthetic maps. Given the similar kinematic structure between the non-LTE and LTE synthetic maps, we conclude non-LTE effects are not important for our analysis and focus on the LTE maps from here on. As this kinematic structure is a robust feature of the simulations, it seems reasonable to compare with the observed ionized gas kinematics.

The morphology of the centroid velocity and second moment maps is similar to the observations; velocity gradients are oriented roughly east–west and velocity dispersion increases towards the centre. A significant difference is that the simulated H II region is smaller (~0.15 pc versus ~0.33 pc), potentially resulting in the steeper velocity gradients compared to the observations due to the conservation of angular momentum.

5 DISCUSSION

As introduced in Section 1, the prior literature looking at the ionized gas kinematics of H II regions has primarily focused on expansion, accretion, and outflows. There are, however, a small number of H II regions in the literature that display velocity gradients perpendicular to the outflow axis. For these regions, a common interpretation is that rotation in some form is contributing to the velocity structure. In Section 5.1, we summarize previous observations put forward as evidence that rotation is playing a role in shaping the velocity gradient. In Section 5.2, we turn to the P10 simulations to try and uncover the origin of the velocity gradient perpendicular to the outflow axis. Section 5.3 refers back to Region 1, discussing whether the velocity structure signifies rotation and what can be inferred with relation to feedback.

5.1 Postulated evidence for rotation in observed H II regions

G34.3+0.2C: Although a cometary H II region, a remarkably strong velocity gradient of ~338 km s^{-1} pc^{-1} has been detected in the H76α RRL, perpendicular to the axis of symmetry. Garay et al. (1986) infer that this could be caused by a circumstellar disc that formed from the collapse of a rotating protostellar cloud. They suggest that the angular velocity of the cloud was a result of Galactic rotation and find that the angle of rotation roughly aligns with that of the Galactic plane. Gaume et al. (1994) refute this since the surrounding molecular material appears to rotate opposite to the ionized gas. Instead, they suggest that stellar winds from two nearby sources have interacted with the ionized gas to give the observed velocity profile.

W49A: Mufson & Liszt (1977) present a low spatial resolution study of W49A and find a velocity range of a few km s^{-1} across the bipolar H II region. In comparison to the velocities of two massive

Table 2. Values for the range in centroid velocity, v_0, velocity gradient, ∇v_0, and maximum velocity dispersion, σ_{max}, for both H II regions in G316.81–0.06, in addition to the LTE and non-LTE simulations of P10 for the final three time-steps.

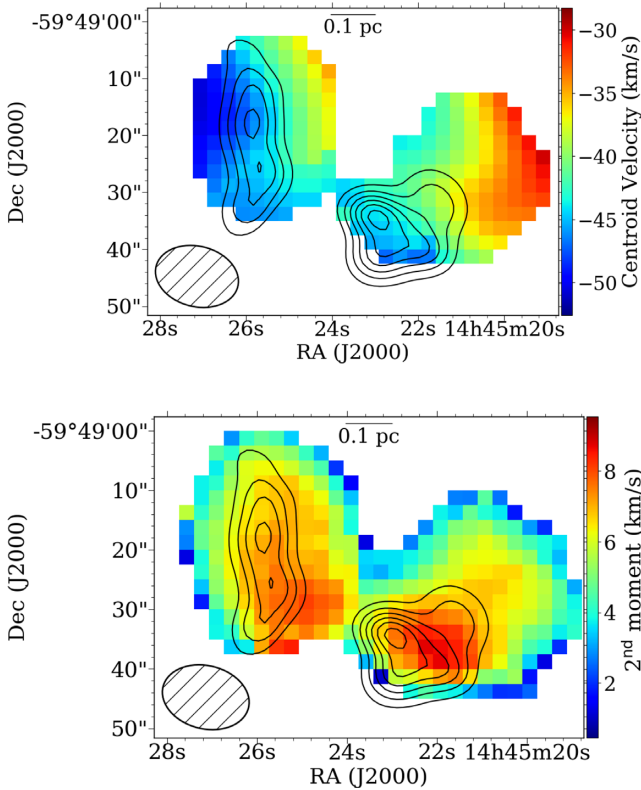| Time (kyr)	Region 1 (E–W)	Region 1 (N–S)	LTE 730.4	LTE 739.2	LTE 746.3	non-LTE 730.4	non-LTE 739.2	non-LTE 746.3
v_0 range (km s^{-1})	15.78 ± 0.45	5.14 ± 1.11	14.59 ± 0.01	11.64 ± 0.01	12.04 ± 0.03	10.49 ± 0.05	10.40 ± 0.12	13.54 ± 0.12
∇v_0 (km s^{-1} pc^{-1})	47.81 ± 3.21	12.23 ± 2.70	97.29 ± 12.97	77.64 ± 10.35	80.25 ± 10.70	69.91 ± 9.33	69.35 ± 9.28	90.28 ± 12.07
σ_{max} (km s^{-1})	8.1	8.1	13.1	12.1	12.1	13.0	11.8	11.8

Figure 6. Maps of the two H II regions within G316.81–0.06: Region 1 (left) and Region 2 (right). Top: centroid velocity map (SCOUSE); bottom: second moment map (CASA). The beam is shown at the bottom left of each map. Contours of the 35-GHz continuum are overlaid in black (Longmore et al. 2009).

molecular clouds on either side of the H II region, they conclude that the ionized gas rotates in the middle of them, as the molecular clouds revolve about one another. With higher spatial resolution, Welch et al. (1987) find a 2-pc ring containing at least 10 separate H II regions that they claim is rotating about 5×10^4 M$_\odot$ of material. They derive an angular velocity of 14.4 km s^{-1} pc^{-1}. With even higher spatial resolution, de Pree, Mehringer & Goss (1997) find 45 distinct continuum sources and that the UCH II regions within the ring do not appear to have ordered motions. However, one UCH II region in particular (W49A/DD), shows a north–south velocity gradient of a few km s^{-1} that de Pree et al. (1997) claim may be caused by the rotation of the ionized gas.

K3-50A: The bipolar H II region, K3-50A, shows a steep velocity gradient ($\sim$150 km s^{-1} pc^{-1}) along the axis of continuum emission, indicating the presence of ionized outflows (de Pree et al. 1994). There also appears to be an unmentioned perpendicular velocity gradient across the region that we estimate to be $\sim$30 km s^{-1} pc^{-1} (see fig. 5a of de Pree et al. 1994). Further detailed comparisons with the

molecular disc have been made (Howard, Koerner & Pipher 1997) in addition to the polarimetry studies (Barnes et al. 2015). This has provided a unique insight to the influence of magnetic fields and allowed for the construction of a detailed 3D model.

NGC 6334A: The velocity gradient of this bipolar H II region was first detected by Rodriguez et al. (1988). de Pree et al. (1995) reconfirmed this, finding a gradient of $\sim$75 km s^{-1} pc^{-1}. They inferred that the signature can be attributed to the rotation of the ionized gas, originating from a circumstellar disc. They derived a core Keplerian mass of $\sim$200 M$_\odot$.

It has also been noted that NGC 6334A, K3-50A, and W49A/A are all alike in terms of their bipolar morphology and the possible presence of ionized outflows (de Pree et al. 1997).

5.2 Origin of the ionized gas velocity structure in the P10 simulations

Since it is difficult for models to take into account all the different physical mechanisms involved with the ionization process, one common simplification is to use static high-mass stars. Such simple analytic models tend to show that ionization occurs isotropically, for a homogeneous surrounding medium, resulting in no velocity gradient. However, in most simulations it is clear that stars are in motion with respect to each other and the surrounding gas.

In the P10 simulations, this motion results in a preferred direction of ionization, downstream of the stellar orbit. We present a simple cartoon (Fig. 9) based on a qualitative examination of the simulated density vector maps (Figs 2 and 3). We find that this can explain the red- and blue-shifted spectra of the observed RRL profile. The cartoon illustrates the evolutionary sequence beginning at the formation of the initial molecular cloud up to the formation of the H II region, explained in more detail by the following:

(i) The initial molecular gas cloud has some net angular momentum (Ω, dashed red arrows), with increasing density towards the centre.

(ii) Once the local critical density of the gas is surpassed, stars (black) form with a high star formation efficiency at the centre of the cloud. The first star forms at the centre of the potential well then quickly drifts outwards, soon followed by the formation of more stars (on time-scales of kyr). These stars all immediately begin to trace the rotation of its natal cloud, about the centre of mass (dashed black arrows).

(iii) The central region starts to become rarefied and a ring-like structure appears (solid red),[3] likely a result of rotational bounce (Cha & Whitworth 2003). Simultaneously, material accumulates about the stars, and new stars form within the dense material and in general continue to trace the rotation of the molecular cloud. The first star makes approximately one complete revolution until

---

[3]We note in passing the similarity to the ring of H II regions in W49A (Section 5.1).
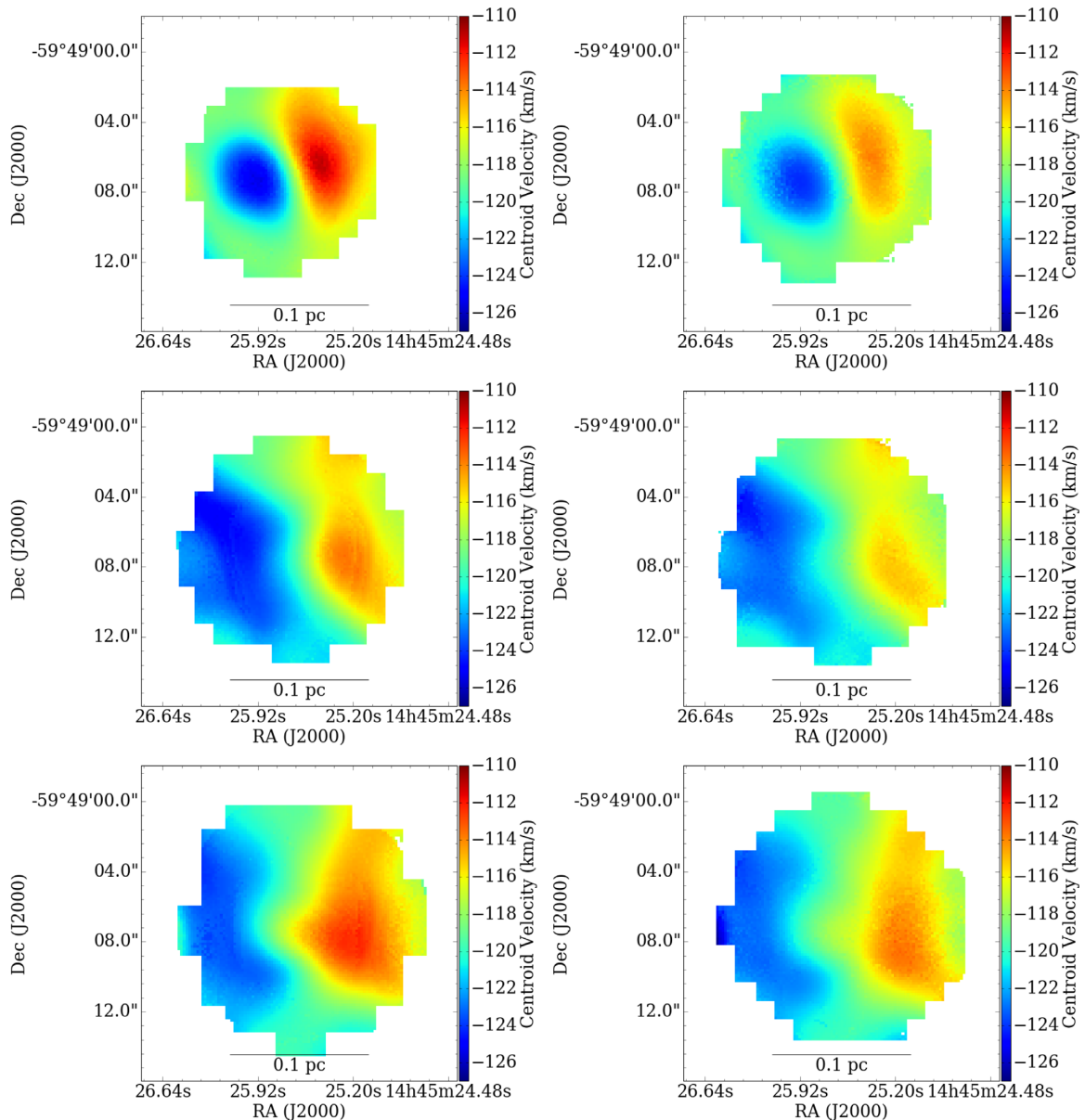
Figure 7. SCOUSE outputted centroid velocity of the simulated H70α data. Left: LTE; right: non-LTE, at ages of 730.4, 739.3, and 746.3 kyr increasing from top to bottom.

the simulation ends (across ∼120 kyr), taking into account that the stars are continually moving outwards as they orbit.

(iv) In the simulations, the rarefied centre is made up of inhomogeneous regions of lower density and lower pressure (shown as solid white for simplicity). Newly ionized material rapidly recombines (also known as flickering; e.g. P10; Galván-Madrid et al. 2011). The stars continue to orbit about the centre of mass and also interact with each other, some getting flung outside the cloud. For a detailed description of stellar cluster formation in this simulation, see Peters et al. (2010c).

(v) Multiple high-mass ionizing stars create one large ionized bubble (solid blue) also containing lower mass stars. The thermal pressure created by ionization heating drives the expansion of the H II region (white arrows), sweeping the surrounding neutral material into a dense shell (thick solid red line). The thermal pressure of the ionized gas is two orders of magnitude higher than in the molecular

gas, and thus the pressure gradient term of the Euler equation dominates over the advection term at the H II region boundary. Hence, the ionized gas does not trace the rotation of the molecular gas directly. The stars act as mediators, inheriting their angular momentum from the molecular gas out of which they formed and then create angular momentum in the ionized gas via a different mechanism (described in more detail next). This is shown by the magnitudes and directions of the velocity arrows of the ionized gas (Fig. 3). If the ionized gas was put in rotation by the surrounding molecular gas, then the arrows on either side of the H II region boundary should always point in the same direction, which is clearly not the case. Furthermore, the varying length of the arrows within the H II region provides evidence for strong dynamical processes inside the H II region that would destroy any such coherent velocity pattern coming from the boundary.
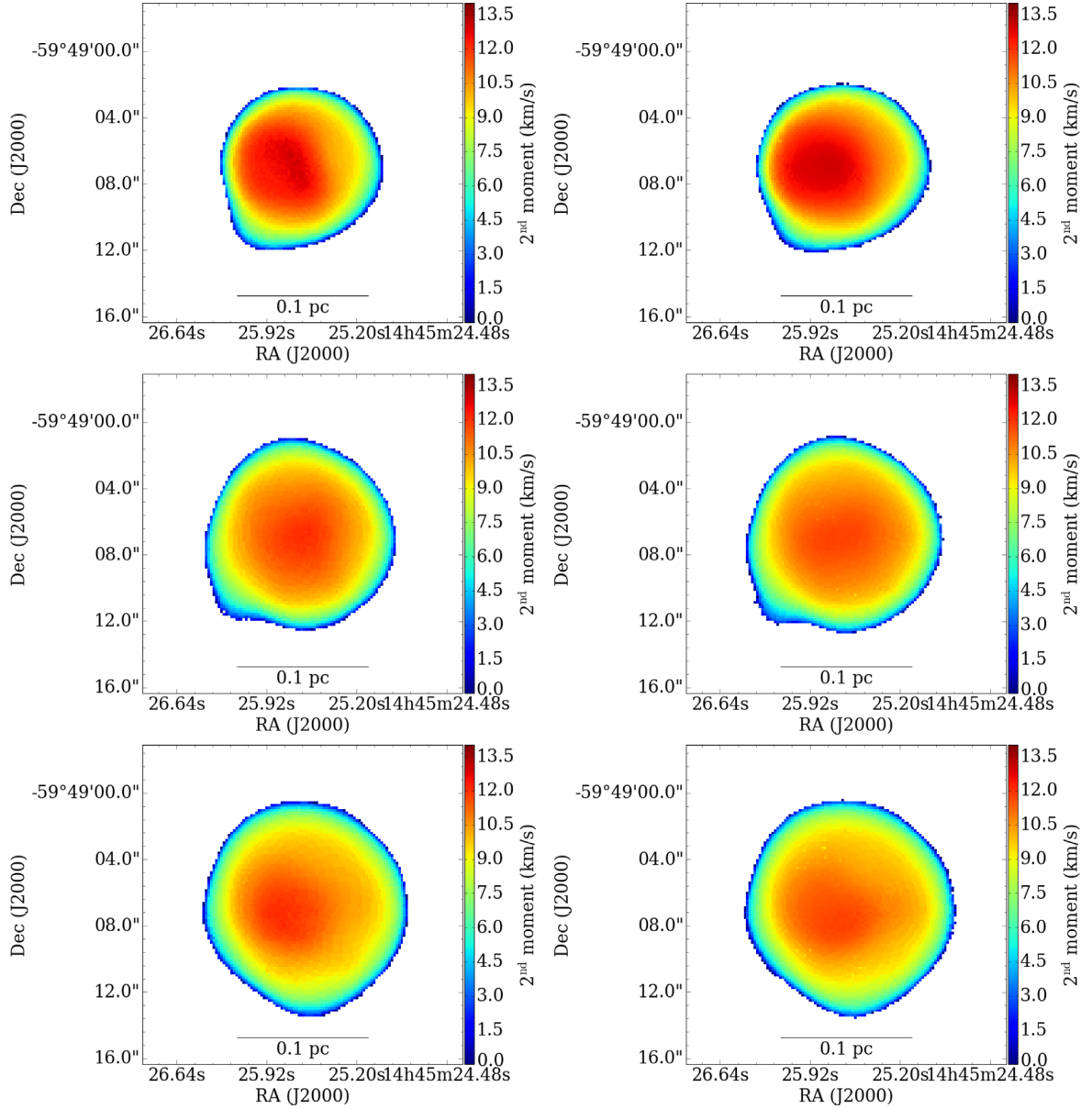
Figure 8. Second moment maps of the simulated H70α data outputted by CASA, showing the velocity dispersion. Left: LTE; right: non-LTE, at ages of 730.4, 739.3, and 746.3 kyr increasing from top to bottom.

In fact, it is these dynamical processes that generate the rotational signature in the ionized gas as follows. Typically, models use an idealized scenario whereby the star is static and ionizes isotropically (e.g. Spitzer 1978). However, in the frame of reference where the star is stationary, consider that upstream of the star's path, the gas flow in the cloud is in opposition to the direction of ionization. This inhibits expansion of the ionized gas, as it is continually replenished by neutral material and recombines. Although downstream of the star's path, the neutral material travels with the direction of ionization; the pressure is lowest ahead of the star in comparison to all other directions. Therefore, the expansion occurs predominantly in front of the star as it orbits, i.e. the path of least resistance. The velocity of the ionized gas traces the orbit of the stars and gas and hence, we observe red- and blue-shifted spectra along our line of sight in the ionized gas of the simulation.

5.3 G316.81–0.06: a rotating H II region?

We now investigate the possible origin of the velocity structure in G316.81–0.06. If it is solely due to outflow and/or expansion of the ionized gas, the bipolar H II region would need to be significantly inclined. Since we clearly observe the elongated 35-GHz continuum and 'green fuzzy' along the axis of bipolarity, in addition to the shallow velocity gradient north–south, we infer that Region 1 is close to edge on, i.e. the line of sight is primarily along the disc plane. While we cannot rule out that the observed velocity structure is caused only by a combination of expansion and outflow, we could not construct a simple model that explains the velocity structure with only these mechanisms. Therefore, we believe that the rotation is the most likely explanation for the velocity gradients.

This is further supported when we compare the ionized gas kinematics in the simulations of P10 to the observations of Region 1.
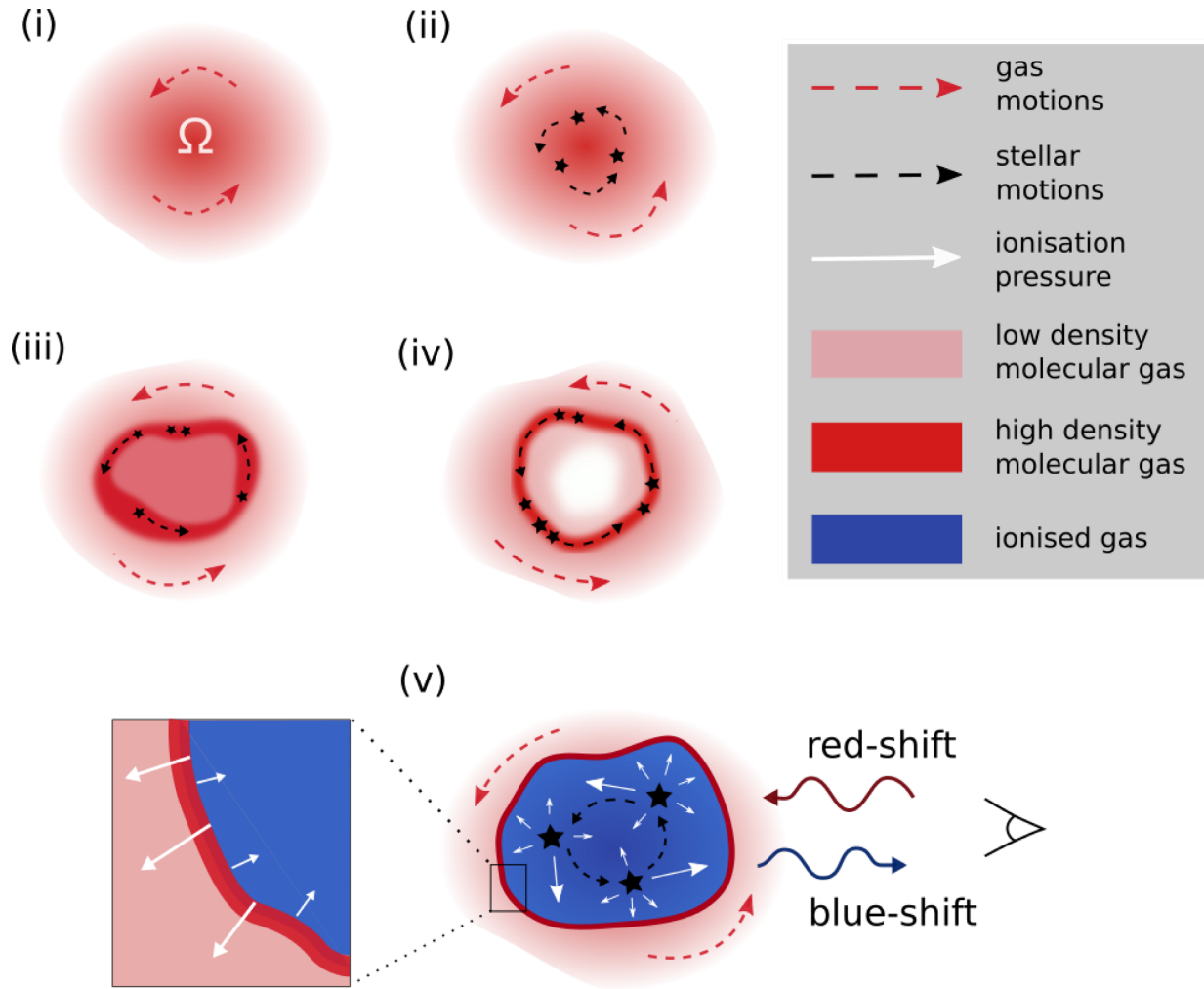
Figure 9. A cartoon illustrating the kinematic evolution of a young H II region. (i) The molecular gas cloud forms with some initial net angular momentum (Ω, dashed red arrows), with increasing density towards the centre of the cloud (pink). (ii) Stars (black) form at the centre of the molecular cloud when the critical density is surpassed, then drift outwards. The stars orbit about the cloud's centre, tracing the angular momentum of the cloud (dashed black arrows). (iii) A ring (solid red) forms as a result of rotational bounce (Cha & Whitworth 2003). Stars continually gain mass and accrete material that gravitationally collects about the stars. The higher density ring initiates the formation of new stars. (iv) The centre becomes rarefied, meanwhile newly ionized material rapidly recombines (also known as flickering). (v) Ionization dominates over recombination resulting in an H II region (blue). Ionization is strongest in the front of the star's path where the pressure is lowest (white arrows). This appears as blue-shifted spectra when the star travels and ionizes towards us, and red-shifted spectra when the star travels and ionizes away from the observer. Molecular material collects about the edge of the ionized region as the bubble expands (thick red solid line).

As shown in Section 4, the morphology is similar, both in terms of centroid velocity and the second moment maps. We also find that the velocity gradient in the simulations is around a factor of two higher than that of Region 1. This may be due to the simulated H II regions being approximately a factor of two smaller (∼0.15 pc as opposed to ∼0.33 pc) and that the inclination of Region 1 may be non-zero.

Further work is needed to explore the significance of rotating gas as opposed to non-rotating gas. In the absence of simulations, fine-tuned to match the observations or higher resolution observations to measure the velocity/proper motions of embedded stars, we have reached the limit of the extent to which we can test this scenario. However, bearing in mind the caveats discussed in Section 2.2, we conclude that the simulations remain a useful tool to aid our understanding of the motions of the ionized gas, especially given the simulations were not fine-tuned to the observations. More-

over, the unusual velocity gradients naturally emerge from the P10 simulations that were not designed to study this effect.

Referring to the previous postulated explanations from Section 5.1, the interpretation of the velocity gradient based on comparison to the P10 simulations is most similar to the scenario put forward by Garay et al. (1986). An interesting prediction of this scenario is that if the initial angular momentum of the cloud is determined by Galactic rotation, the magnitude of rotation will depend on the location in the Galaxy, and the orientation of the angular momentum axis with reference to the Galactic plane.

Although not included in the P10 simulations, another possible explanation for the rotation of G316.81–0.06 may be due to the IRDC, clearly seen in Fig. 1. Accretion from the filament would likely induce some net angular momentum on to a central core. Watkins et al. (in preparation) are currently studying the molecular gas kinematics of G316.81–0.06. Their results will allow for a

detailed comparison between the motions of ionized and molecular gas in order to test this scenario.

If either scenario can describe the origin of the ionized gas motions in many H II regions, similar velocity gradients should also be evident in RRLs for other young (bipolar) H II regions. In order to test the scenario of rotation induced by filamentary accretion, comparative studies between the kinematics of H II regions and IRDCs are required. Galactic plane surveys, with upcoming and highly sensitive interferometers (e.g. EVLA- and SKA-pathfinders), will provide a high-resolution census of all ionized regions in the Milky Way. These H II regions will be at different locations in the Galaxy, with different orientations and magnitudes of angular momentum with respect to Earth. We will have an invaluable test bed at the earliest and poorly understood phases of star formation, allowing for the study of RRLs in H II regions across a large range of ages, sizes, and morphologies. Future high- resolution observational surveys in combination with suites of numerical simulations will also further our understanding of the differing contributing feedback mechanisms at early evolutionary stages and may help to constrain different star/cluster formation scenarios.

For example, the simulations of P10 can give an idea of which feedback mechanism(s) have an important effect in G316.81–0.06. The simulations include both heating by ionizing and non-ionizing radiation, where the latter's only effect is to increase the Jeans mass (see discussion in Peters et al. 2010c). Therefore, all dynamical feedback effects in the simulation are due to photoionization. This may imply that ionization pressure is the dominating feedback mechanism required for the formation of a rotating ionized gas bubble and that radiation pressure and protostellar outflows are not needed to explain the dynamical feedback. This is potentially present in all H II regions and needs to be studied further in other simulations that incorporate different feedback mechanisms. Although the formation and evolution of galaxies will not be significantly different whether or not the outflowing gas is rotating, the potential to use the ionized gas kinematics as a tracer to identify very young H II regions represents an opportunity to understand feedback at the relatively unexplored time-/size scales when the stars are just beginning to affect their surroundings on cloud scales.

6 SUMMARY

We have studied a rare example of a young, bipolar H II region that shows a velocity gradient in the ionized gas, perpendicular to the bipolar-continuum axis. Through comparisons of our H70α RRL observations with the synthetic data of P10, we find that they both share a similar morphology and velocity range along the equivalent axis.

We infer that the velocity gradient of G316.81–0.06 is the rotation of the ionized gas, and that the simulations demonstrate that this rotation is a direct result of the initial net angular momentum of the natal molecular cloud. Further tests are required to deduce the origin of this angular momentum, whether it is induced by Galactic rotation, filamentary accretion, or other. If rotation is a direct result of some initial net angular momentum, this observational signature should be common and routinely observed towards other young H II regions in upcoming radio surveys (e.g. SKA, SKA-pathfinders, EVLA). Further work is required to know if velocity gradients are a unique diagnostic.

If rotation is seen to exist in other H II regions, and we can uncover its true origins, this may help to parametrize the dominating feedback mechanisms at early evolutionary phases, greatly demanded by numerical studies. This should be achievable through systematic

studies of many H II regions, combined with comparison to a wider range of numerical simulations, likely offering a new window to this investigation.

REFERENCES

Agertz O., Kravtsov A. V., 2016, ApJ, 824, 79
Agertz O., Kravtsov A. V., Leitner S. N., Gnedin N. Y., 2013, ApJ, 770, 25
Anaconda 2017, Anaconda Software Distribution (v.1–1.8.7), https://anaconda.com
Astropy Collaboration, 2013, A&A, 558, A33
Barnes P. et al., 2015, MNRAS, 453, 2622
Batchelor R. A., Caswell J. L., Haynes R. F., Wellington K. J., Goss W. M., Knowles S. H., 1980, Aust. J. Phys., 33, 139
Battersby C., Bally J., Jackson J. M., Ginsburg A., Shirley Y. L., Schlingman W., Glenn J., 2010, ApJ, 721, 222
Benjamin R. A. et al., 2003, PASP, 115, 953
Beuther H., Churchwell E. B., McKee C. F., Tan J. C., 2007, in Reipurth V. B., Jewitt D., Keil K., eds, Protostars and Planets V. Univ. Arizona Press, Tucson, AZ, p. 165
Beuther H., Walsh A. J., Longmore S. N., 2009, ApJS, 184, 366
Breen S. L., Ellingsen S. P., Caswell J. L., Lewis B. E., 2010a, MNRAS, 401, 2219
Breen S. L., Caswell J. L., Ellingsen S. P., Phillips C. J., 2010b, MNRAS, 406, 1487
Busfield A. L., Purcell C. R., Hoare M. G., Lumsden S. L., Moore T. J. T., Oudmaijer R. D., 2006, MNRAS, 366, 1096
Butler M. J., Tan J. C., Teyssier R., Rosdahl J., Van Loo S., Nickerson S., 2017, ApJ, 841, 82
Carey S. J. et al., 2009, PASP, 121, 76
Caswell J. L., 1998, MNRAS, 297, 215
Caswell J. L., 2009, PASA, 26, 454
Caswell J. L., Haynes R. F., 1987, Aust. J. Phys., 40, 215
Caswell J. L., Vaile R. A., Ellingsen S. P., 1995a, PASA, 12, 37
Caswell J. L., Vaile R. A., Ellingsen S. P., Whiteoak J. B., Norris R. P., 1995b, MNRAS, 272, 96
Caswell J. L., Vaile R. A., Ellingsen S. P., Norris R. P., 1995c, MNRAS, 274, 1126
Cha S.-H., Whitworth A. P., 2003, MNRAS, 340, 91
Chambers E. T., Jackson J. M., Rathborne J. M., Simon R., 2009, ApJS, 181, 360
Christensen L. L., Nielsen L. H., Nielsen K. K., Johansen T., Hurt R., de Martin D., 2012, Astrophysics Source Code Library, record ascl:1206.002
Churchwell E. et al., 2009, PASP, 121, 213
Cole S., Lacey C. G., Baugh C. M., Frenk C. S., 2000, MNRAS, 319, 168
Cyganowski C. J. et al., 2008, AJ, 136, 2391
Dale J. E., Ercolano B., Bonnell I. A., 2013, MNRAS, 430, 234
de Pree C. G., Goss W. M., Palmer P., Rubin R. H., 1994, ApJ, 428, 670
de Pree C. G., Rodriguez L. F., Dickel H. R., Goss W. M., 1995, ApJ, 447, 220
de Pree C. G., Mehringer D. M., Goss W. M., 1997, ApJ, 482, 307

de Pree C. G., Wilner D. J., Deblasio J., Mercer A. J., Davis L. E., 2005, ApJ, 624, L101

de Pree C. G. et al., 2014, ApJ, 781, L36

de Pree C. G. et al., 2015, ApJ, 815, 123

Deharveng L. et al., 2015, A&A, 582, A1

Dullemond C. P., Juhasz A., Pohl A., Sereshti F., Shetty R., Peters T., Commercon B., Flock M., 2012, Astrophysics Source Code Library, record ascl:1202.015

Egan M. P., Shipman R. F., Price S. D., Carey S. J., Clark F. O., Cohen M., 1998, ApJ, 494, L199

Fischler M. A., Bolles R. C., 1981, Commun. ACM, 24, 381

Fryxell B. et al., 2000, ApJS, 131, 273

Galván-Madrid R., Rodríguez L. F., Ho P. T. P., Keto E., 2008, ApJ, 674, L33

Galván-Madrid R., Peters T., Keto E. R., Mac Low M.-M., Banerjee R., Klessen R. S., 2011, MNRAS, 416, 1033

Garay G., Rodriguez L. F., van Gorkom J. H., 1986, ApJ, 309, 553

Gaume R. A., Claussen M. J., 1990, ApJ, 351, 538

Gaume R. A., Fey A. L., Claussen M. J., 1994, ApJ, 432, 648

Giannetti A., Leurini S., Wyrowski F., Urquhart J., Csengeri T., Menten K. M., König C., Güsten R., 2017, A&A, 603, A33

Girichidis P., Federrath C., Banerjee R., Klessen R. S., 2011, MNRAS, 413, 2741

Girichidis P. et al., 2016, MNRAS, 456, 3432

Gordon M. A., Sorochenko R. L., 2002, in Burton W. B. et al., Astrophysics and Space Science Library, Vol. 282, Radio Recombination Lines:Their Physics and Astronomical Applications. Springer, Netherlands, p. 91

Green J. A., McClure-Griffiths N. M., 2011, MNRAS, 417, 2500

Green J. A. et al., 2012, MNRAS, 420, 3108

Gutermuth R. A., Heyer M., 2015, AJ, 149, 64

Haworth T. J., Glover S. C. O., Koepferl C. M., Bisbas T. G., Dale J. E., 2017, NAR, preprint (arXiv:1711.05275v5)

Helfand D. J., Becker R. H., White R. L., Fallon A., Tuttle S., 2006, AJ, 131, 2525

Henshaw J. D. et al., 2016, MNRAS, 457, 2675

Hoare M. G. et al., 2012, PASP, 124, 939

Hopkins P. F., Kereš D., Oñorbe J., Faucher-Giguère C.-A., Quataert E., Murray N., Bullock J. S., 2014, MNRAS, 445, 581

Hou L. G., Han J. L., 2014, A&A, 569, A125

Howard E. M., Koerner D. W., Pipher J. L., 1997, ApJ, 477, 738

Immer K., Cyganowski C., Reid M. J., Menten K. M., 2014, A&A, 563, A39

Inkscape Team 2015, Inkscape, https://inkscape.org

Jupyter Notebook 2018, Project Jupyter, https://jupyter.org

Juvela M., 1996, A&AS, 118, 191

Katz N., Weinberg D. H., Hernquist L., 1996, ApJS, 105, 19

Kaufmann P. et al., 1976, Nature, 260, 306

Kennicutt R. C., Evans N. J., 2012, ARA&A, 50, 531

Kereš D., Katz N., Davé R., Fardal M., Weinberg D. H., 2009, MNRAS, 396, 2332

Keto E., 2002, ApJ, 568, 754

Keto E., 2003, ApJ, 599, 1196

Keto E., 2007, ApJ, 666, 976

Keto E., Klaassen P., 2008, ApJ, 678, L109

Keto E., Wood K., 2006, ApJ, 637, 850

Keto E. R., Ho P. T. P., Haschick A. D., 1988, ApJ, 324, 920

Kim C.-G., Ostriker E. C., Kim W.-T., 2013, ApJ, 776, 1

Kim W.-J., Wyrowski F., Urquhart J. S., Menten K. M., Csengeri T., 2017, A&A, 602, A37

Klaassen P. D., Wilson C. D., Keto E. R., Zhang Q., 2009, ApJ, 703, 1308

Klaassen P. D., Galván-Madrid R., Peters T., Longmore S. N., Maercker M., 2013, A&A, 556, A107

Klaassen P. D. et al., 2018, A&A, 611, A99

Klessen R. S., Heitsch F., Mac Low M.-M., 2000, ApJ, 535, 887

Krumholz M. R., Cunningham A. J., Klein R. I., McKee C. F., 2010, ApJ, 713, 1120

Krumholz M. R. et al., 2014, in Beuther H., Klessen R. S., Dullemond C. P., Henning T., eds, Protostars and Planets VI. Univ. Arizona Press, Tucson, AZ, p. 243

Longmore S. N., Burton M. G., Barnes P. J., Wong T., Purcell C. R., Ott J., 2007, MNRAS, 379, 535

Longmore S. N., Burton M. G., Keto E., Kurtz S., Walsh A. J., 2009, MNRAS, 399, 861

Longmore S. N. et al., 2017, MNRAS, 470, 1462

Lumsden S. L., Hoare M. G., 1996, ApJ, 464, 272

Lumsden S. L., Hoare M. G., 1999, MNRAS, 305, 701

MacLeod G. C., Gaylard M. J., 1992, MNRAS, 256, 519

McGee R. X., Gardner F. F., Robinson B. J., 1967, Aust. J. Phys., 20, 407

McMullin J. P., Waters B., Schiebel D., Young W., Golap K., 2007, in Shaw R. A., Hill F., Bell D. J., eds, ASP Conf. Ser. Vol. 376, Astronomical Data Analysis Software and Systems XVI. Astron. Soc. Pac., San Francisco, p. 127

Mufson S. L., Liszt H. S., 1977, ApJ, 212, 664

Muratov A. L., Kereš D., Faucher-Giguère C.-A., Hopkins P. F., Quataert E., Murray N., 2015, MNRAS, 454, 2691

Murray N., Ménard B., Thompson T. A., 2011, ApJ, 735, 66

Myers A. T., Krumholz M. R., Klein R. I., McKee C. F., 2011, ApJ, 735, 49

Núñez A., Ostriker J. P., Naab T., Oser L., Hu C.-Y., Choi E., 2017, ApJ, 836, 204

Pestalozzi M. R., Minier V., Booth R. S., 2005, A&A, 432, 737

Peters T., Banerjee R., Klessen R. S., Mac Low M.-M., Galván-Madrid R., Keto E. R., 2010a, ApJ, 711, 1017 (P10)

Peters T., Mac Low M.-M., Banerjee R., Klessen R. S., Dullemond C. P., 2010b, ApJ, 719, 831

Peters T., Klessen R. S., Mac Low M.-M., Banerjee R., 2010c, ApJ, 725, 134

Peters T., Longmore S. N., Dullemond C. P., 2012, MNRAS, 425, 2352

Peters T., Klaassen P. D., Mac Low M.-M., Schrön M., Federrath C., Smith M. D., Klessen R. S., 2014, ApJ, 788, 14

Peters T. et al., 2017, MNRAS, 466, 3293

Robitaille T., Bressert E., 2012, Astrophysics Source Code Library, record ascl:1208.017

Rodriguez L. F., Bastian T. S., 1994, ApJ, 428, 324

Rodriguez L. F., Moran J. M., Canto J., Kahn F. D., 1988, Bull. Am. Astron. Soc., 20, 1031

Scannapieco C. et al., 2012, MNRAS, 423, 1726

Sewiło M., Churchwell E., Kurtz S., Goss W. M., Hofner P., 2008, ApJ, 681, 350

Shaver P. A., Retallack D. S., Wamsteker W., Danks A. C., 1981, A&A, 102, 225

Sollins P. K., Zhang Q., Keto E., Ho P. T. P., 2005, ApJ, 624, L49

Somerville R. S., Primack J. R., 1999, MNRAS, 310, 1087

Spitzer L., 1978, Physical Processes in the Interstellar Medium. Wiley, New York

Springel V., Hernquist L., 2003, MNRAS, 339, 312

Tanaka K. E. I., Tan J. C., Zhang Y., 2016, ApJ, 818, 52

Tasker E. J., Wadsley J., Pudritz R., 2015, ApJ, 801, 33

Urquhart J. S. et al., 2013a, MNRAS, 431, 1752

Urquhart J. S. et al., 2013b, MNRAS, 435, 400

Veena V. S., Vig S., Tej A., Kantharia N. G., Ghosh S. K., 2017, MNRAS, 465, 4219

Walsh A. J., Hyland A. R., Robinson G., Burton M. G., 1997, MNRAS, 291, 261

Walsh A. J., Burton M. G., Hyland A. R., Robinson G., 1998, MNRAS, 301, 640

Walsh A. J. et al., 2011, MNRAS, 416, 1764

Walsh A. J., Purcell C. R., Longmore S. N., Breen S. L., Green J. A., Harvey-Smith L., Jordan C. H., Macpherson C., 2014, MNRAS, 442, 2240

Welch W. J., Dreher J. W., Jackson J. M., Terebey S., Vogel S. N., 1987, Science, 238, 1550

Wood D. O. S., Churchwell E., 1989, ApJS, 69, 831

APPENDIX A:

Table A1. Masers found in close proximity to G316.81−0.06.

RA (J2000)	Dec. (J2000)	Maser type	v_{peak} (km s^{-1})	References
14 45 26.6	−59 49 14	Hydroxyl	−36.7	McGee, Gardner & Robinson (1967)
14 45 27.6	−59 49 49	Hydroxyl	−41	Caswell & Haynes (1987)
14 45 26.34	−59 49 15.4	Hydroxyl	−44	Caswell (1998)
14 45 26.34	−59 49 15.4	Hydroxyl	−43.5	Breen et al. (2010b)
14 45 27.6	−59 49 49	Class II methanol	−44	MacLeod & Gaylard (1992)
14 45 27.9	−59 49 13	Class II methanol	−42.1	Caswell, Vaile & Ellingsen (1995a)
14 45 27.9	−59 49 13	Class II methanol	−46.8	Caswell et al. (1995b)
14 45 27.9	−59 49 13	Class II methanol	−45.7	Caswell et al. (1995c)
14 45 28	−59 49 12	Class II methanol	−46.0	Walsh et al. (1997)
14 45 26.44	−59 49 16.3	Class II methanol	−42.2	Walsh et al. (1998)
14 45 26.44	−59 49 16.5	Class II methanol	−44.9	Walsh et al. (1998)
14 45 26.44	−59 49 16.4	Class II methanol	−45.8	Walsh et al. (1998)
14 45 26.44	−59 49 16.3	Class II methanol	−46.9	Walsh et al. (1998)
14 45 26.44	−59 49 16.3	Class II methanol	−48.1	Walsh et al. (1998)
14 45 26.4	−59 49 16.5	Class II methanol	−46.0	Pestalozzi, Minier & Booth (2005)
14 45 26.4	−59 49 16.3	Class II methanol	−46.3	Caswell (2009)
14 45 26.4	−59 49 16.3	Class II methanol	−46.3	Breen et al. (2010b)
14 45 26.4	−59 49 16.3	Class II methanol	−45.8	Green et al. (2012)
14 45 30.3	−59 51 52	Water	−48.6	Kaufmann et al. (1976)
14 45 25.0	−59 49 31	Water	−46	Batchelor et al. (1980)
14 45 26.58	−59 49 14.1	Water	−46	Breen et al. (2010b)
14 45 25.5	−59 49 18	Water	−47.2	Walsh et al. (2011)
14 45 26.1	−59 49 19.5	Water	−50.6	Walsh et al. (2014)
14 45 26.4	−59 49 15.3	Water	−45.5	Walsh et al. (2014)
14 45 26.4	−59 49 15.2	Water	−40.9	Walsh et al. (2014)
14 45 26.4	−59 49 15.5	Water	−39.2	Walsh et al. (2014)
14 45 26.4	−59 49 15.4	Water	−34.6	Walsh et al. (2014)

This paper has been typeset from a TeX/LaTeX file prepared by the author.